Free-Surface Effects in 3D Dislocation Dynamics: Formulation and Modeling

Tariq A. Khraishi

Department of Mechanical Engineering,
University of New Mexico,
Albuquerque, NM 87131
e-mail: khraishi@me.unm.edu

Hussein M. Zbib

School of Mechanical
and Materials Engineering,
Washington State University,
Pullman, WA 99164
e-mail: zbib@mme.wsu.edu

Recent advances in 3-D dislocation dynamics include the proper treatment of free surfaces in the simulations. Dislocation interaction and slip is treated as a boundary-value problem for which a zero-traction condition is enforced at the external surfaces of the simulation box. Here, a new rigorous method is presented to handle such a treatment. The method is semi-analytical/numerical in nature in which we enforce a zero traction condition at select collocation points on a surface. The accuracy can be improved by increasing the number of collocation points. In this method, the image stress-field of a subsurface dislocation segment near a free surface is obtained by an image segment and by a distribution of prismatic rectangular dislocation loops padding the surface. The loop centers are chosen to be the collocation points of the problem. The image segment, with proper selection of its Burgers vector components, annuls the undesired shear stresses on the surface. The distributed loops annul the undesired normal stress component at the collocation points, and in the process create no undesirable shear stresses. The method derives from crack theory and falls under "generalized image stress analysis" whereby a distribution of dislocation geometries or entities (in this case closed rectangular loops), and not just simple mirror images, are used to satisfy the problem's boundary conditions (BCs). Such BCs can, in a very general treatment, concern either stress traction or displacements. [DOI: 10.1115/1.1479694]

1 Introduction

There has been a great deal of interest in the literature with regard to treating the interaction of dislocations with nearby free surfaces. As it turns out, this is a classical problem of interest and importance in dislocation theory. For example, it is known that for an infinite screw dislocation situated near a free half-plane, another screw dislocation of opposite sign and mirror position is needed to annul the stress traction on the surface. The effect of the free surface in this simple but illustrative case is evident. Here, the closer the subsurface dislocation is to the free surface, the stronger (and faster) it gets pulled to the surface by the image dislocation, assisting in its fast removal from within the crystal; bringing back the order of the atomic arrangement. For an infinite edge dislocation near a free half-plane, the image dislocation problem is much more complicated than the simple mirror solution of a screw dislocation even though, configurationally, this is still a simple problem.

Since near-surface dislocation is a problem of importance, several researchers have investigated different aspects of it, and tackled it in different ways. Initially, Yoffe [1] determined the elastic fields of a dislocation half-line terminating at a free surface of an isotropic elastic body for any angle of incidence and any Burgers vector. Bacon and Groves [2] and Groves and Bacon [3] obtained the displacements of an infinitesimal dislocation loop of arbitrary orientation residing in a semi-infinite isotropic elastic medium. The elastic field of a closed finite or semi-infinite dislocation loop can thus be obtained by means of area integration using the results for the infinitesimal loop. Maurissen and Capella [4,5] derived the stress fields of a dislocation segment (and half-line) parallel and perpendicular to a free surface of a semi-infinite isotropic medium, respectively. Concurrently with the works of Maurissen and Capella [4,5] Comninou and Dundurs [6] found the elastic fields associated with an angular dislocation in an elastic isotropic half

space. They remarked that the fields of any polygonal loop could be constructed by superposition using their results. For an arbitrary dislocation in an isotropic, homogenous half-space, Gosling and Willis [7] have expressed the stresses as a line integral around the dislocation. For the special case of a dislocation half-line, the integral was evaluated analytically to yield closed form solutions for the stresses. These in turn can be used to find the stresses of a line-segment in the half-space. The aforementioned solution is rather difficult to use and implement. Later in the paper, we propose an alternative treatment. Finally, Lothe et al. [8] developed an integral expression for the case of a dislocation terminating at the free surface of an anisotropic half-space. In this work they solved the problem by a planar fan-shaped distribution of infinite straight dislocations which replaced the condition of a free surface. This idea is similar to solving crack problems by the proper distribution of stress sources (i.e., dislocation entities).

2 Overview of 3-D Dislocation Dynamics (DD)

A discrete dislocation dynamics (DD) model, *micro3d*, has recently been developed by Zbib et al. [9] and Rhee et al. [10]. The DD model is a powerful tool for investigating the mechanical response of materials on a mesoscopic scale. In a DD simulation, the plastic deformation of a single crystal is obtained by explicit accounting of the dislocation evolution history, i.e., their motion and structure. The motion and interaction of an ensemble of dislocations in a three-dimensional crystal is integrated in time.

A typical simulation domain is a box of 5-30 μm side length. Dislocations are discretized into straight-line segments, and the stress field produced by each segment is calculated. There are two commonly used explicit expressions for the stress field of a dislocation line segment. One is given by Hirth and Lothe [11] using local or body-fixed coordinate system, and the other is provided by DeVincre [12] with respect to a global coordinate system. Direct reference to a global coordinate system eliminates the intermediate step of stress tensor transformation, something that, intuitively, should reduce the computational effort.

The Peach-Koehler force **F** acting on a dislocation segment inside the computational cell is calculated from the stress fields

due to immediate neighboring segments, all other dislocations, all other crystal defects, and the applied stress. The force per unit line length acting on segment i is expressed as:

$$F_i = \left(\left(\sum_{\substack{j=1, j \neq i, \\ j \neq i+1, j \neq i-1}}^{N} \sigma_j^D + \sigma^a \right) \cdot b_i \right) \times \xi_i + F_{i,i+1} + F_{i,i-1}. \quad (1)$$

Here, the superscript a refers to applied stresses, the last two terms in the equation represent closest neighbors' contributions, σ_j^D represent the contribution of all other segments evaluated at the midpoint of segment i, b_i is the Burgers vector, and ξ_i is the line sense.

The result is used to advance the dislocation segment based on a linear mobility model:

$$v_{gi} = M_{gi} F_{gi} \quad (2)$$

where v_{gi} is the glide velocity of the ith dislocation segment, M_{gi} is the dislocation mobility, and F_{gi} is the glide component of the Peach-Koehler force. In this equation, F_{gi} represents the *net* force causing glide after subtracting out the Peierls friction. Notice here that the glide force, F_{gi}, represents the projection of the force **F** in the direction of the in-plane normal to the segment. Generally, M_{gi} is, among other things, a function of the dislocation character, especially at low temperatures.

Based on the history of dislocation motion, one obtains a macroscopic measure for the plastic strain rate tensor $\mathbf{D^P}$ as

$$\mathbf{D^p} = \sum_{i=1}^{N} \frac{-l_i v_{gi}}{2V} (n_i \otimes b_i + b_i \otimes n_i), \quad (3)$$

where $n_i = v_{gi} \times \xi_i$ is the unit normal to the slip plane of segment i, l_i is the segment length, $\mathbf{V}$ is the volume of the simulated crystal, and N is the total number of dislocation segments. In the DD code, only volume-conserving plastic deformation resulting from dislocation slip is incorporated so far. On the other hand, nonvolume-conserving motion of dislocations (e.g., dislocation climb) is not implemented. The stress rate is determined from Hooke's law:

$$\dot{\sigma} = \lfloor \mathbf{C^e} \rfloor (D - D^p) \quad (4)$$

where $[\mathbf{C}^e]$ is the elasticity tensor, and **D** is the total strain rate tensor.

In the simulation, segments that are on the verge of experiencing short-range interactions are identified. Based on a set of physical rules, such reactions may result in the formation of junctions, jogs, dipoles, etc. The dislocations multiply by a variety of mechanisms that may involve jog collisions, standard Frank-Read source multiplication, and double cross slip. More details regarding the DD model can be found in the previous articles (Zbib and co-workers, [9,10]).

3 Theoretical Development

Consider Fig. 1 showing a subsurface dislocation segment (segment $A_1 B_1$) in a computational cell representing a specimen of a single-crystal material. Here, *XYZ* represent a globally fixed coordinate system. Without loss of generality, one can ascribe a local coordinate system *xyz* to the free surface, as Fig. 2 illustrates. Here, **i**, **j**, and **k** are an orthonormal basis for the Cartesian space, **n** is a unit vector normal to the surface, **b** is the Burgers vector associated with the segment, t_1 is the line sense vector of the segment. The condition of zero traction requires that the stress vector, **T**, associated with any surface point, P, is identically equal to zero. In other words, we must have $T = \sigma n = 0$. This translates to the condition: $\sigma_{xz} = \sigma_{yz} = \sigma_{zz} = 0$, at surface points. In order to ensure no shear stresses at these points, it can be shown that a simple image construction across the surface (i.e., segment $A_2 B_2$ in Fig. 2, which is a mirror reflection of segment $A_1 B_1$), with the proper selection of the Burgers vector components, suffices to accomplish this task. In particular, this can be achieved by
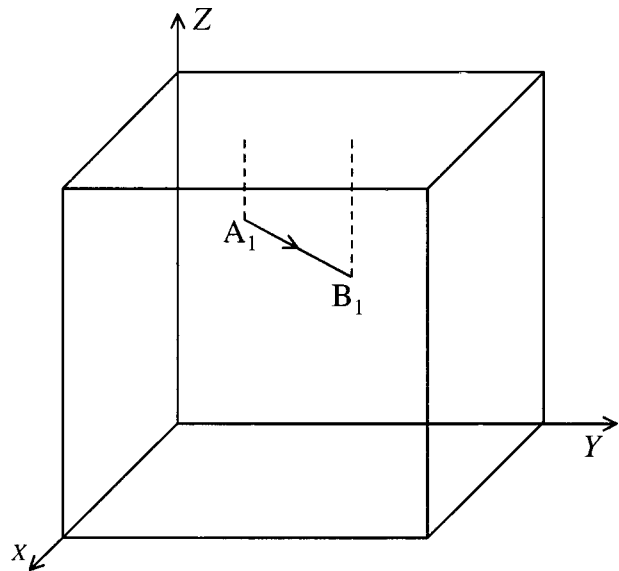

Fig. 1 A dislocation segment inside a computational box

setting $b_z^{A_2 B_2} = b_z^{A_1 B_1}$, $b_x^{A_2 B_2} = -b_x^{A_1 B_1}$, and $b_y^{A_2 B_2} = -b_y^{A_1 B_1}$. This can be proven after some careful analysis (details skipped) of the stress fields associated with the two mirror segments. Formulas for such fields are available in Hirth and Lothe [11], and Devincre [12]. This image solution, however, does not annul the σ_{zz} component of stress. In fact, this component turns out to be additive for both segments at any surface point. The unannulled σ_{zz} component of these two segments together represent a continuous function of x and y, $f(x,y)$, on the surface's plane. To annul this component of stress, there does not seem to be (at least intuitively) a simple image construction that would do so without causing shear stresses. Hence to annul σ_{zz} component, a different treatment is needed.

To annul the σ_{zz} component, consider surface **S** in Fig. 3 on which such annulment is desired. This surface represents a certain portion of the total surface area, which can be small or big (up to the total original surface area to which it belongs). Lets further subdivide **S** into N number of smaller square (or rectangular) surface elements. The purpose of such division is to annul the σ_{zz} component in a discrete fashion by requiring it to be identically zero at the centers of these elements. The satisfaction of such a requirement over all elements does not necessarily ensure its satisfaction at other surface points besides the centers of the elements. Therefore this technique is numerical and approximate in character. More accuracy can be attained by further subdividing **S** into an increasingly larger number of elements (i.e., using smaller and smaller elements). This further subdivision of **S** works in
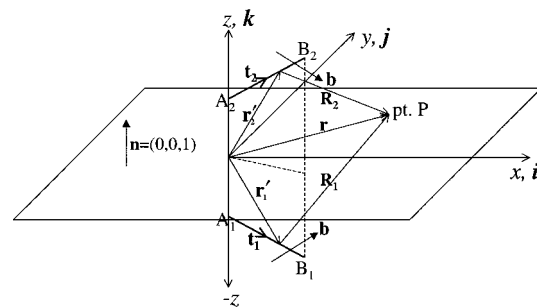

Fig. 2 Segment $A_1 B_1$ beneath a surface with ascribed local coordinate system
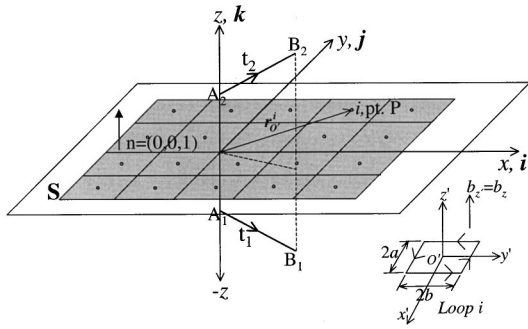
Fig. 3 A mesh of rectangular elements, representing prismatic dislocation loops, covering area S upon which surface traction annulment is sought. The inset shows one of these prismatic dislocation loops.

effect to ensure the satisfaction of the boundary condition at more and more points on the surface (covering the whole surface in the limit).

So far, nothing has been said on how to achieve the nullification of the σ_{zz} component at the midpoints, or centers, of the surface's square (or rectangular) N elements. To accomplish this purpose, we propose to treat these elements as dislocation entities; in harmony with the idea of "generalized image stress analysis" discussed earlier. In particular, we propose to treat them as prismatic dislocation loops. Figure 3 shows one of these rectangular dislocation loops, termed *Loop i*, illustrating its line sense and perpendicular Burgers vector with respect to a local or body-fixed coordinate system $x'y'z'$. The center of this loop in global xyz coordinates is $(x_{O'}^i, y_{O'}^i, z_{\mathbf{O'}}^i)$. The stress field of such prismatic loops can be derived by integration of the Peach-Koehler equation, which expresses the stress field of an arbitrary curved dislocation in terms of a line integral (see the following). Alternatively, one can find the stress field of the loop as the additive sum, from the principal of superposition, of the four dislocation segments composing it. The stress field of a dislocation segment is given in Hirth and Lothe [11] and in Devincre [12] as discussed earlier.

From studying the characteristics of these prismatic loops, say using the $x'y'z'$ coordinate system, it turns out that at the center of these loops the only nonvanishing component of loop stress (from among σ_{xz}, σ_{yz}, σ_{zz}) is the σ_{zz} component. In the current context, the center of the loops can be considered as Gaussian points at which determination of numerical quantities (in this case stress) is desired. Based on the above, the annulment of the σ_{zz} component of stress at the center of any loop, i, (in the presence of the segment and its image) can be stated as follows:

$$\sigma_{zz}^i = -\sum_{\substack{j=1 \\ j \neq i}}^{N} \sigma_{zz}^j - \sigma_{zz}^{A_1 B_1} - \sigma_{zz}^{A_2 B_2}, \qquad i = 1 \cdots N, \qquad (5)$$

where σ_{zz}^j is the stress associated with *Loop j* (evaluated of course at the center of *Loop i*), $\sigma_{zz}^{A_1 B_1}$ is the stress associated with segment $A_1 B_1$, $\sigma_{zz}^{A_2 B_2}$ is the stress associated with segment $A_2 B_2$. Note that the unknown in each of the terms in Eq. (5) is the magnitude of the perpendicular or z-component of the Burgers vector (b_z) of the dislocation loops. For each of these stress terms, this component of $\mathbf{b}$ premultiplies some other terms or kernels (i.e., it's a separable coefficient of the stress terms corresponding to the loops in (5)). Hence, for each loop, i, Eq. (5) corresponds to a linear relationship between N unknowns; representing the unknown b_z magnitudes of the loops. Applying Eq. (5) N times at the centers of all loops produces a set of N linear algebraic equations that can be conventionally solved using whatever system solver of choice.

Note that the above devised numerical scheme is self-consistent geometrically, numerically, and within the context of dislocation theory. Note also that the extent of area $\mathbf{S}$ upon which the boundary condition is enforced is a problem parameter and can be extended almost indefinitely. Finally, note that the choice of dislocation loops to annul any undesirable surface tractions is advantageous. This is because the stress field of such loops rapidly decays (i.e., as $1/r^3$, where r is the distance from the dislocation core). Therefore, the loop distribution on an external surface, say representing one of the boundaries of a finite computational cell, will have little effect on the tractions on other nearby surfaces (which will be perpendicularly oriented in the case of a cubic cell). In other words, an assumption of uncoupling in the image treatment of the different surfaces would not be far fetched here. The accuracy of the above scheme for a given area size $\mathbf{S}$ can be improved, as discussed earlier, using finer meshing (i.e., larger N, or smaller and smaller loop sizes).

Consider Eq. (5) again. Notice that it can be rewritten as follows:

$$\sum_{j=1}^{N} \sigma_{zz}^j = -\sigma_{zz}^{A_1 B_1} - \sigma_{zz}^{A_2 B_2}, \qquad i = 1 \cdots N, \qquad (6)$$

where it is understood that evaluation of quantities in (6) is done at the center of the loop in question (i.e., *Loop i*). Now let the area of each of the discretizing loops tend to an infinitesimal value, dA'. Obviously, for a given surface $\mathbf{S}$, infinitely many such small loops will be needed to cover it. Each of these infinitesimal loops has associated with it an infinitesimal Burgers vector directed along the z-axis (i.e., db_z'). The distribution of these Burgers vectors naturally introduces a density function defined on the xy-plane, $B(x', y')$, such that (at a given surface point) $db_z' = B(x', y')dA'$. This is equivalent to stating that $B(x', y') = db_z'/dA'$. Hence, the summation in (6) can be replaced with an integral, and one can instead write:

$$\int_S B(x', y') K(x - x', y - y') dA' = -\sigma_{zz}^{A_1 B_1} - \sigma_{zz}^{A_2 B_2}, \qquad (7)$$

where $K(x - x', y - y')$ is the kernel of the stress term associated with the infinitesimal loop located at (x', y') and discussed previously. Now, assuming $B(x', y')$ to be piecewise area constant, i.e., constant in value over N finite area elements, one can further write:

$$\int_S B(x', y') K(x - x', y - y') dA'$$

$$= \sum_{j=1}^{N} \int_{A^j} B(x', y') K(x - x', y - y') dA'$$

$$= \sum_{j=1}^{N} B^j \int_{A^j} K(x - x', y - y') dA', \qquad (8)$$

where A^j is the area of element j.

Furthermore, the integral in Eq. (8) can be evaluated to first order as follows:

$$\int_{A^j} K(x - x', y - y') dA' = K(x - x_{O'}^j, y - y_{O'}^j) A^j. \qquad (9)$$

In Eq. (9), the evaluation of the kernel is done at the center of element or *Loop j*. Finally, observing that $B^j A^j = b_z^j$, one can see that combining this observation with Eqs. (9), (8), and (7), Eq. (6) results. Hence, the original statement of Eq. (5) represents a special case of (7). Notice that although (7) is the more general statement of the problem, the equivalent statement, Eq. (5), was arrived at intuitively. The form of Eq. (7) is analogous to crack

problems (see, e.g., Hills et al. [13]) which utilize a distribution or pileup of dislocations to annul undesirable tractions on a crack's face.

4 The Stress Field of a Rectangular Prismatic Dislocation Loop

As the section before explained, one needs to know the stress field of a rectangular prismatic dislocation loop. For one thing, the σ_{zz} stress component of such a loop is needed in the annulment of traction forces as prescribed by Eq. (6). Furthermore, once the b_z's for all surface loops are determined, one would need to calculate all the stress components by these loops, along with the stresses induced by the image segment A_2B_2, at the center of segment A_1B_1 in order to evaluate the Peach-Koehler force acting on it.

To derive the stress field of a rectangular prismatic dislocation loop, one needs to integrate the Peach-Koehler (PK) contour integral for the loop geometry described in the inset of Fig. 3. The PK equation is a line or contour integral that sums the stresses of differential dislocation line elements as one traverses a closed loop (of any curvature or shape) in the direction of the dislocation's line sense. The dislocation can have three components of the Burgers vector and the integration can be carried out with respect to any coordinate system, in principle.

The PK equation is given by the following (see Hirth and Lothe [11]):

$$\sigma_{\alpha\beta} = -\frac{G}{8\pi} \oint_C b_m$$

$$\in_{im\alpha} \frac{\partial}{\partial x_i'} \nabla'^2 R dx_\beta' - \frac{G}{8\pi} \oint_C b_m$$

$$\in_{im\beta} \frac{\partial}{\partial x_i'} \nabla'^2 R dx_\alpha' - \frac{G}{4\pi(1-\nu)} \oint_C b_m$$

$$\in_{imk} \left(\frac{\partial^3 R}{\partial x_i' \partial x_\alpha' \partial x_\beta'} - \delta_{\alpha\beta} \frac{\partial}{\partial x_i'} \nabla'^2 R \right) dx_k' \quad (10)$$

where b_i is the (ith component of the) Burgers vector, $\in$ is the permutation symbol, G is the shear modulus, and ν is Poisson's ratio. The prime, used as a superscript, indicates quantities belonging to a traced differential line segment $d\mathbf{l}'$ of the dislocation loop. The vector $\mathbf{R}$, with magnitude $R = |\mathbf{R}|$, is the difference vector between the position vector of $d\mathbf{l}'$ (i.e., $\vec{r}' = (x', y', z')$) and position vector of a field point P (i.e., $\vec{r} = (x, y, z)$,) i.e., $\mathbf{R} = \vec{r}' - \vec{r}$.

To perform the integration, the indices in (10) should first be expanded. This gives six independent equations, one for each stress component ($\sigma_{x'x'}$, $\sigma_{y'y'}$, $\sigma_{z'z'}$, $\sigma_{y'z'}$, $\sigma_{x'z'}$, and $\sigma_{x'y'}$), corresponding to a permutation of the α and β indices from 1 to 3. We also note that the dislocation loop is chosen to lie in the xy plane (i.e., $z' = 0$), and that $\nabla'^2 R = 2/R$. In what follows, we omit the lengthy integration steps for brevity and simply provide the final result in the Appendix (for details on the integration process, the reader is referred to other previous work by the authors, e.g., Khraishi et al., [14,15]). Note in the Appendix that a stands for half of the loop's side length in the x-direction (see Fig. 3), and b is half the side length in the y-direction.

5 Numerical Implementation of the Problem

An alternative form for Eq. (6) is:

$$\sum_{j=1}^{N} \sigma_{zz}^j = -2\sigma_{zz}^{A_1B_1}, \qquad i = 1 \cdots N, \quad (11)$$

where the 2 in the right-hand side of the equation comes from the fact that the contributions of segments A_1B_1 and A_2B_2 are equal.

Knowing that the σ_{zz} stress component of a prismatic loop is equal to a b_z multiplying a kernel $K(x,y)$, when $z=0$ (see Appendix), and that $\sigma_{zz}^{A_1B_1}$ evaluated in the plane under consideration (i.e., $\mathbf{S}$ or the collocation points' plane) is also a function of x and y only, one can express the last equation as:

$$\sum_{j=1}^{N} b_z^j K(x_{O'}^i - x_{O'}^j, y_{O'}^i - y_{O'}^j) = -2\sigma_{zz}^{A_1B_1}|_{\text{center of Loop } i}$$

$$= -f(x_{O'}^i, y_{O'}^i) i = 1 \cdots N. \quad (12)$$

For simplicity and without loss of generality, if one chooses the sub-plane segment and its mirror image to lie in the xz-plane, one can then write the function $f(x,y)$, using DeVincre's expression (Devincre [12]), as:

$$f(x,y) = 2(\sigma_{zz}^*|_{r_{B_1}'} - \sigma_{zz}^*|_{r_{A_1}'}), \quad (13)$$

$$\sigma_{zz}^*|_{r'} = \frac{G}{\pi Y^2} \left[\begin{array}{c} 2(b_x Y_y - b_y Y_x) t_z + \dfrac{2b_y Y_z t_x}{1-\nu} \\ -\dfrac{\text{term}^*}{1-\nu}[(b_y Y_z - b_z Y_y)t_x + (b_x Y_y - b_y Y_x)t_z] \end{array} \right],$$

$$r' = (x', y' = 0, -z'),$$

$$Y_x = (x - x') + Rt_x, Y_y = y, Y_z = z' + Rt_z, Y = \sqrt{Y_x^2 + Y_y^2 + Y_z^2},$$

$$R = \sqrt{(x-x')^2 + y^2 + z'^2}, \quad (14)$$

$$\text{term}^* = 1 + t_z^2 + \frac{2Y_z}{Y^2}\left[2(z' - Lt_z) + \frac{L}{R}Y_z \right],$$

$$L = (x - x')t_x + z't_z.$$

For a square prismatic loop (i.e., $a = b$), the σ_{zz} stress component evaluated in the plane of the loop (i.e., $z = 0$) simplifies to the following form:

$$\sigma_{zz} = b_z K(x,y)$$

$$= \frac{Gb_z}{4\pi(1-\nu)}$$

$$\times \left(\begin{array}{c} \dfrac{\sqrt{(a-x)^2 + (a-y)^2}}{(a-x)(a-y)} + \dfrac{\sqrt{(a+x)^2 + (a-y)^2}}{(a+x)(a-y)} \\ + \dfrac{\sqrt{(a-x)^2 + (a+y)^2}}{(a-x)(a+y)} + \dfrac{\sqrt{(a+x)^2 + (a+y)^2}}{(a+x)(a+y)} \end{array} \right). \quad (15)$$

Here, $K(x,y)$ is the sought after kernel in Eq. (12)

Considering Eq. (12), one can see that N equations corresponding to N collocation points will be generated. The collocation points correspond to N rectangular prismatic surface loops with unknown b_z's. Hence we have at hand an $N \times N$ system of linear algebraic equations:

$$\underbrace{[A]}_{N \times N} \underbrace{\{b_z\}}_{N \times 1} = \underbrace{\{C\}}_{N \times 1}, \quad (16)$$

In (16), the $[A]$ matrix contains the interacting kernels and the $\{C\}$ vector is like a forcing vector that contains the negatives of the function $f(x,y)$. This system of equations can be written in expanded form if desired but is skipped here for brevity. By examining the expanded form, it turns out that the $[A]$ matrix is fully-populated, symmetric (for equally-sized square loops), and diagonally dominant. The fully-populated feature is self explanatory. The symmetry feature is due to the fact that for a square prismatic loop i, its kernel evaluated at the center of loop j is exactly equal to the kernel of j evaluated at the center of i. Finally, the matrix is diagonally dominant because its kernel evalu-

ated at its own center is much larger in magnitude than when it is evaluated at other loops' centers. As a matter of fact, the kernel decays as $1/r^3$.

6 Results and Discussion

In the previous chapter, we have developed the theoretical and numerical treatments for the problem of a subsurface dislocation segment (segment A_1B_1). The problem was solved using an image dislocation segment A_2B_2 (of fixed Burgers vector) and a distribution of N rectangular prismatic dislocation loops padding the surface area in question. Here, the treatment leads to a linear system of algebraic equations the solution of which is the Burgers vectors of the surface loops. Once the Burgers vectors of the surface loops are known, one can compute the Peach-Koehler force at the center of the segment A_1B_1 as follows:

$$F^{A_1B_1} = \left(\left(\sum_{i=1}^{N} \sigma^i + \sigma^a + \sigma^{A_2B_2} \right) \cdot b^{A_1B_1} \right) \times \xi^{A_1B_1}. \quad (17)$$

In Eq. (17), the superscripts a and A_2B_2 refer to the applied stresses and the image segment stresses, respectively. The summation in the above equation accumulates the effects of all N surface loops (as mentioned earlier, the stress field of a loop is given in the Appendix). Note that the quantities in Eq. (17) can be first evaluated with respect to a local or surface-attached coordinate system and then transformed back to a global reference frame. Note that based on physical intuition, the Peach-Koehler force acting on a subsurface segment (Eq. (17)) tends to pull the segment toward the surface in order to minimize the crystal energy.

Now in a finite simulation box as the ones typically considered in 3-D DD studies, a segment in the box theoretically feels, to a greater or lesser extent, the effect of the different surfaces bounding the box. There are six surfaces in a cubical computational domain. To quantify the effect of each of these surfaces on an enclosed segment, using the above-described method, the box surfaces are padded or meshed with square surface loops. This is depicted in Fig. 4. Each of the surfaces is numbered for identification and a local coordinate system is attached to it. Notice that our global coordinate system is located at the center of the box.

Now every segment in the box is reflected across the different external surfaces as shown in Fig. 5. This provides for image segments using the above-described method. Each one of these surfaces, of course, is padded with square dislocation loops as alluded to earlier. Once all of the above is in place, the surface effect on a segment is the summation of the effect of *all* six external surfaces, calculated separately one at a time. To reiterate, we calculate the Peach-Koehler force on a segment from each of
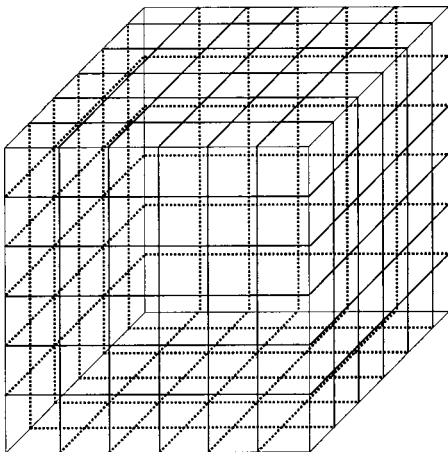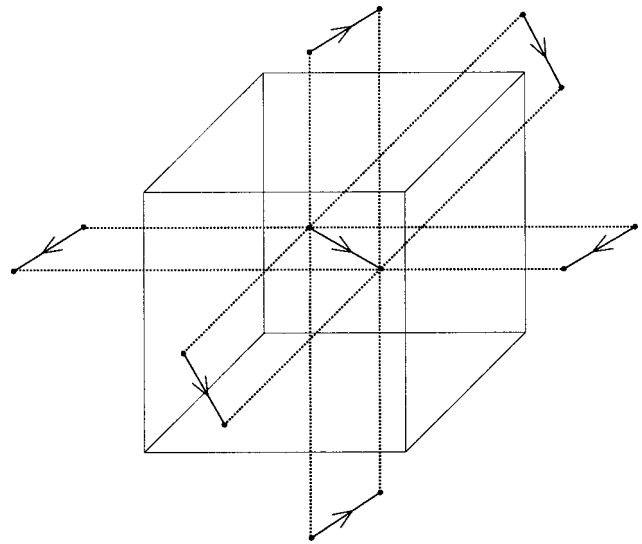

Fig. 5 A dislocation segment in a DD computational box reflected off of the six external box surfaces

the surfaces individually and independently, and later sum up their contributions. This amounts to solving *six* linear systems of equations for local b_z's corresponding to each of the surfaces. All of this has been implemented in the *micro3d* DD code. A variety of results using this implementation have been obtained and are presented below.

It is appropriate here to mention that, given the limits of elasticity theory, the force on a subsurface segment can only be calculated to within a core distance or depth (i.e., z-depth $= 0.5b$-$4b$) from the surface. This is in harmony with other DD calculations which take this limitation into account and deal with it similarly. This has to be taken into account, otherwise the dislocation segment might overlap the core of surface dislocation loop; an invitation for numerical problems! This is not a serious limitation by any means, as we will see later, because the force acting to pull the segment toward the surface at these small depths is tremendously high and causes the rapid vanishing of such segments.

A note now on the solution of the linear system of algebraic equations (Eq. (16)) is in order. To solve this system one can choose a solver of personal preference. For example, one can choose the Gauss-elimination method with partial pivoting and scaling (see Chapra and Canale [16]). Now due to the fact that the $[A]$ matrix in (16) is diagonally dominant, one can be assured convergence, if an iterative method like the Gauss-Seidel method with relaxation (see also the last reference) is chosen. Iterative methods are known to be much faster than traditional Gauss-elimination, especially for solving a large system of equations, and can thus result in substantial timesavings. In addition, the precision of the final solution (i.e., the number of significant digits) is controllable when using iterative methods. More details on these issues, if needed, can be found in Khraishi [17]. Finally, it is worth mentioning that both methods have been tried and produce identical results as expected.

In order to test the above treatment of traction-free surfaces, the most trivial study case is that of a subsurface screw dislocation segment that is parallel to the plane. Here the subsurface segment had a length equal to the finite surface area dimension in the y-direction. The solution to this scenario has been compared with the solution provided by Maurissen and Capella [4] for a horizontal segment beneath a half-plane. It turns out that both solutions are identical (not shown here for brevity). The reason for this is trivial and it is because the screw horizontal segment does not create any undesirable σ_{zz} stresses on the surface in need of an-

Fig. 4 Faces of a DD computational box uniformly meshed with square elements representing prismatic dislocation loops

nulment. This leads to a zero $\{b_z\}$ vector in the solution of (16). In other words, the solution for a subsurface horizontal screw dislocation segment is simply the image segment solution and is valid over the whole half-plane and not just the finite surface area. This is identical to the treatment of infinitely long screw dislocation lines parallel to the surface.

More comparisons between our solution for horizontal and vertical segments beneath a finite surface area have been made with the solution provided by Maurissen and Capella for a half-plane. At the outset, one needs to recognize that the two solutions will not match due to area size differences. However, if one chooses a large enough area, and a small enough segment away from the area corners and close to the finite plane, one should expect a good resemblance between the two solutions. This is understandable because such a situated segment would "see" the large finite area as if it were infinite! In all of the results below, the segment length L, the shear modulus G, and Poisson ratio ν, were set equal to $100b$, 42.25 Gpa, and 0.383, respectively.

Consider first a vertical subsurface segment A_1B_1. Segment A_1B_1 lies along the negative z-axis. The line sense vector, however, points in the positive z-direction, i.e., $\xi=(0,0,1)$. The coordinates of A_1 and B_1 are $(0,0,-1100b)$ and $(0,0,-1000b)$, respectively. The Burgers vector has two nonzero components $\mathbf{b}=(1/\sqrt{3},0,1/\sqrt{3})$. This choice of nonzero Burgers vector components corresponds to the choice made by Maurissen and Capella in their work. The finite surface area $\mathbf{S}$ represents a square with a side of $20,000b$. If one compares the σ_{xx}, σ_{yy}, and σ_{zz} components using the above method with the method of Maurissen and Capella for an area division of 10×10 intervals, i.e., 10 intervals along a side totaling 100 surface loops, one gets Fig. 6. In this plot, the field or evaluation points are chosen to lie along an axis parallel to the y-axis with $x=0$, and at a depth of $400b$ from the surface.

In Fig. 6, the stresses obtained by the two methods follow similar trends but noticeably differ in value. Perhaps this is due to the relatively low loop density (i.e., coarse mesh) used in conjunction with the current solution. Therefore, one remedy might be to increase the meshing density, i.e., decrease the loop size and therefore decrease the spacing between the collocation points on the surface. Intuitively speaking, increasing the number of collocation points on a given surface should improve the performance of the

Fig. 7 Same as Fig. 6 but with a surface mesh density of 30×30 loops.

current solution. Figure 7 illustrates this idea using the higher density of 30×30 loops. In this figure we notice that the agreement between the two methods is better than before but is still not so great. If one increases the meshing density further as was done in Fig. 8 using a 50×50 division, one sees that the two methods give almost identical results. Increasing the meshing density further will only enhance the agreement between the stress components obtained using the two methods (the plots from the two methods will perfectly collapse on one another).

Two comments are in order regarding Figs. 6-8. First, it is noted that the agreement between the current solution and that by Maurissen and Capella reached a climax, roughly, in Fig. 8 for which there were 50×50 loops padding the surface (note that 50×50 is the largest mesh density of surface loops used here). This meshing density translates roughly to an average separation distance of about $400b$ in between the collocation points. Incidentally, this is the same subsurface depth chosen for the evaluation points in the figures. This should come to no surprise if one reviews the premise of the current method. Here we are seeking the annulment of σ_{zz} stresses at the traction-free surface. We are achieving this in a discrete manner by enforcing compliance with the boundary condition at selected collocation points (which happen to be the surface loops' centers in this case). This problem is basically an elasticity problem and its solution has been formulated in that context. St. Venant's Principle of elasticity theory, however, states that agreement between an exact solution and an approximate, but
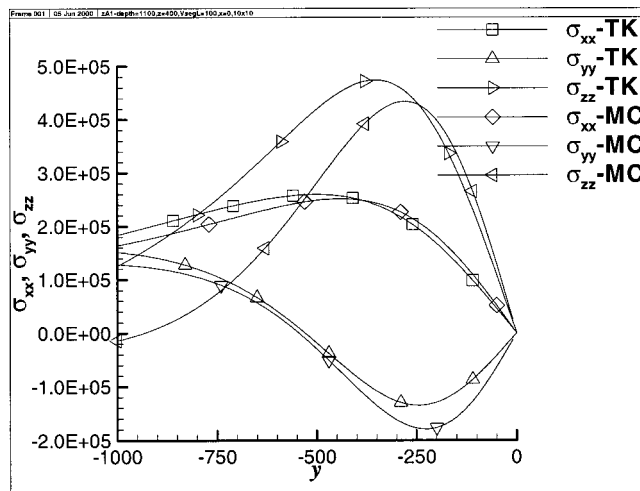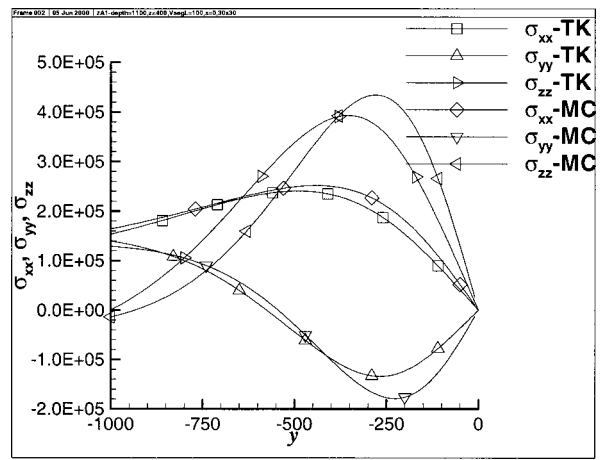

Fig. 6 Comparisons of the stresses from the current work (TK) versus the work by Maurissen and Capella (MC) for a subsurface vertical segment. Stresses are in Pa. The segment points in the positive z-direction, has a zero y-component of b, and a length of $100b$. The stresses are plotted along an axis parallel to the y-axis at a depth of $400b$. The surface is $20,000b$ on each side and has a mesh density of 10×10 loops.
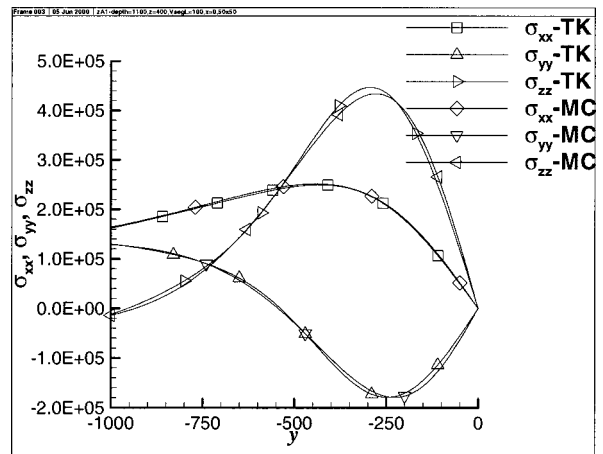

Fig. 8 Same as Fig. 6 but with a surface mesh density of 50×50 loops

functionally equivalent, one at a boundary will be achieved if one considers field points that lie more than a "characteristic" distance away from the boundary. The characteristic distance in this case can be thought of as the average separation distance between collocation points where the boundary condition is enforced. As the meshing density is increased and the characteristic distance is decreased one expects that our approximate numerical solution will coincide with the exact solution in the limit.

Now if one plots instead the variation σ_{xy}, σ_{xz}, and σ_{yz} along the same axis as before, one would basically get similar results to the σ_{xx}, σ_{yy}, and σ_{zz} cases described earlier, i.e., good agreement between the current solution and that of Maurissen and Capella. Figures are not shown here for brevity. Hence, it seems that the current solution, so far, checks very well against other existing solutions in the literature.

Now if one evaluates the stresses at depths from the surface less than the average separation distance between the collocation points, one would see oscillations in the plotted curves. These oscillations are an inherent feature of the current solution and can be annihilated by simply increasing the mesh density to the extent that the average separation distance between collocation point is equal or less than the field points depth. Also, if one determines a least squares high-degree polynomial fit for the oscillatory curves, one finds out that the oscillations occur about the correct behavior (i.e., they closely resemble the solution by Maurissen and Capella) and are not oscillating vigorously. It is noticed here that the period of the oscillations is equal to the average separation distance between the collocation points and that the oscillation amplitude diminishes with increasing mesh density. More on this and plots illustrating this phenomenon can be found with reference to Khraishi et al. [18] and Khraishi [17].

Finally, it must be mentioned that if one instead compares the Maurissen and Capella's solution for a *horizontal* segment instead of a vertical segment with the current method introduced in this paper, one would also find satisfactory agreement. This was done in Khraishi et al. [18] and Khraishi [17].

More results can be obtained that tend to support the current method. For example, consider a subsurface horizontal dislocation segment A_1B_1. As the depth of the segment decreases, i.e., the segment approaches the surface, the Peach-Koehler force pulling it toward the surface should accordingly increase. In other words, there is an inverse relationship between the Peach-Koehler force-pull toward the surface and the segment depth. Figure 9 supports this physical intuition. In addition, as the dislocation segment length increases, the Peach-Koehler force acting on it and coming
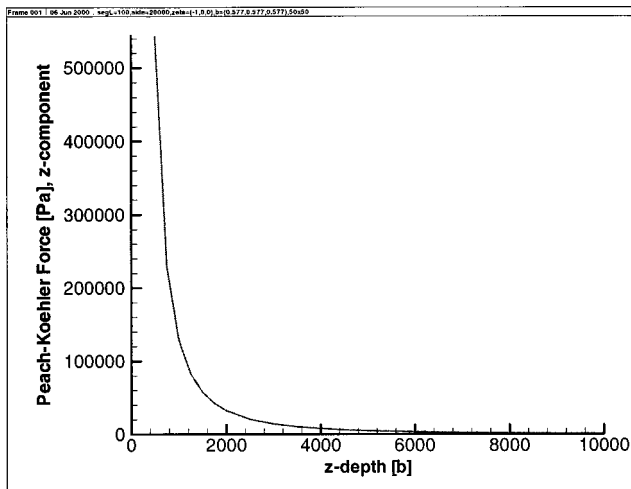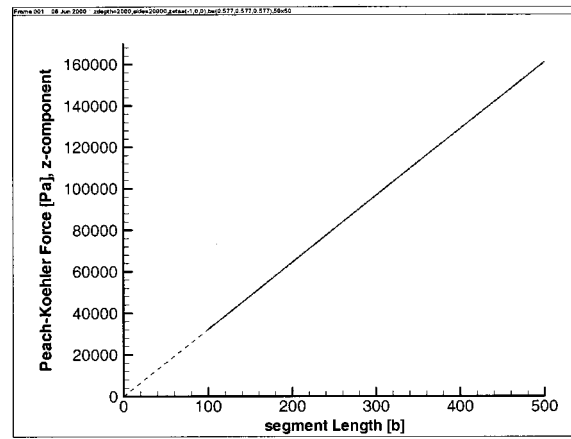

Fig. 10 The Peach-Koehler force pulling a subsurface horizontal segment towards the surface versus the segment length for a fixed segment depth

from the image stress analysis, should also increase because the segment has a "stronger presence" now. Figure 10 is a plot of the force pulling the segment toward the surface versus the segment length. One can see that the plot is meaningful, since it extrapolates back to zero as the segment length completely diminishes.

Finally, some results from incorporating the above method of treating traction-free surfaces into the *micro3d* DD code are exhibited. Figure 11 show stress-strain diagrams obtained from DD simulations for cubic specimens 10,000b in size containing a dislocation source close to one of the external surfaces. The specimen was subjected to a tensile straining rate of $10 \, s^{-1}$. In the figure, a case of no surface loops (i.e., no treatment of the boundary condition) is compared to cases of surface padding of 10×10, 20×20, and 30×30 loops. In this figure, one can clearly notice the surface effect. Here the curves with boundary condition treatment saturated at a higher stress than the curve obtained with no surface loops. This is understandable since the dislocation source is close to an exterior surface, thus it is difficult to propagate dislocations away from this nearby surface (part of a typical Frank-Read
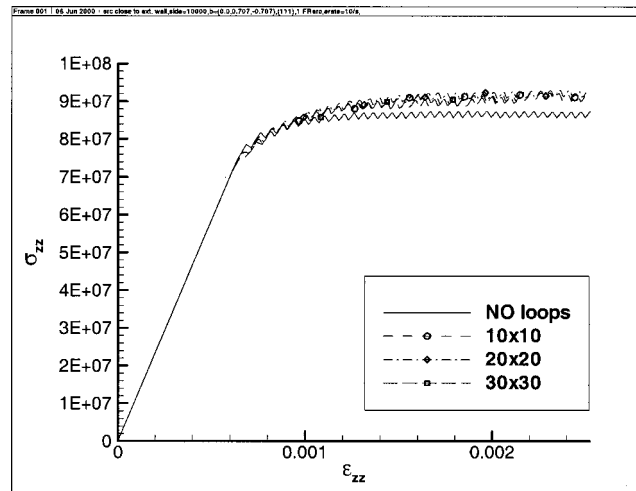

Fig. 9 The Peach-Koehler force pulling a subsurface horizontal segment towards the surface versus the segment depth for a fixed segment length

Fig. 11 Stress-strain diagrams from DD simulations for one operational Frank-Read source in a cubic cell that is 10,000b in side length. The source is close to the cell's external surfaces. The continuous line correspond to no treatment of the traction-free boundary condition, and the dashed lines corresponds to an external surface mesh density of 10×10 loops, 20×20 loops, and 30×30 loops.

source action) thus reducing the extent of plastic flow for a given applied stress. In other words, as the source tries to operate normally as it would by emitting dislocation loops, it is held back by the attraction of the nearby free surface. The effect of this is to cause a higher saturation level for the cases with surface loops as opposed to the case with no loops. If the dislocation source were located to the interior of the simulation cell however, far away from surface effects predictably, one would notice the reverse effect to what is above. In particular, the saturation level of the stress-strain curve for the surface-treated case would be at a lower level than that with no surface treatment. This is to be expected since the surfaces would here assist in the operation of the source and the glide of dislocation segments as opposed to hindering them. Such a result was presented earlier by Khraishi et al. [18].

7 Conclusions

This work presents a numerical treatment of the dislocation image stress problem applicable to three-dimensional dislocation dynamics (DD). The method meshes the external surfaces of the DD computational box with prismatic dislocation loops (which are fictitious dislocations used as mathematical convenience to provide auxiliary self-equilibrated stress terms in the problem formulation). By utilizing "image" dislocation segments and finding the Burgers vectors of the surface prismatic loops, one can satisfy the traction-free boundary condition at select collocation points (taken here as the loops' centers although they don't have to be) on the computational box's external surfaces.

There are few things to notice about the current method. First, it is computationally intensive adding to the $O(\text{N}^2)$ that dislocation dynamics naturally poses. This is not a major drawback since the method can be accelerated using parallel processing techniques, and because of nowadays Gegahertz computer processor speeds.

Second, there are other methods to treat traction-free boundary conditions within the context of dislocation dynamics. The finite-element method (FEM) is popular in this regard. The advantage of this method over the FEM is that here there is no need to specify displacement boundary conditions (which might not be appropriate in some instances) to compute a numerical solution. Another advantage is that in the FEM, one has to solve for displacements at the FE nodes in a 3D spatial nodal array although the desired result from the solution is a derived one (i.e., stress values). In this context then, this would represent an extra step that is not fully utilized in the final analysis.

Third, very close to the corners of the computational box, the numerical solution calculated here is not completely accurate. This is due to the use of the image dislocation segments since they help annul shear stresses on their symmetry surfaces but not on orthogonal ones at the corners. This also is not a major drawback since instances of dislocation segments in corner regions are probabilistically small. Therefore, their effect on the total stress solution is inherently minimized.

Fourth and last, it is worth noting that the solution methodology presented in this work is applicable to anisotropic as well as isotropic elasticity problems. However, calculating the stresses of in-the-box dislocation segments using anisotropic elasticity theory is an endeavor far from being trivial and the dynamic analysis of the problem would pose an even more formidable task.

Appendix

The stress components of a rectangular prismatic dislocation loop of side lengths $2a$ and $2b$ along the x and y-directions, respectively, are:

$$\sigma_{xx}=\frac{-Gb_z}{2\pi}\left(\begin{array}{l}\frac{(-a+x)(-b+y)}{((-b+y)^2+z^2)\sqrt{(-a+x)^2+(-b+y)^2+z^2}}-\frac{(a+x)(-b+y)}{((-b+y)^2+z^2)\sqrt{(a+x)^2+(-b+y)^2+z^2}}\\[2mm]-\frac{(-a+x)(b+y)}{((b+y)^2+z^2)\sqrt{(-a+x)^2+(b+y)^2+z^2}}+\frac{(a+x)(b+y)}{((b+y)^2+z^2)\sqrt{(a+x)^2+(b+y)^2+z^2}}\end{array}\right)\frac{-Gb_z}{4\pi(1-\nu)}$$

$$\times\left(\begin{array}{l}-\frac{(-a+x)(-b+y)(2(-a+x)^2+(-b+y)^2+z^2)}{((-b+y)^2+z^2)((-a+x)^2+(-b+y)^2+z^2)^{3/2}}+\frac{(a+x)(-b+y)(2(a+x)^2+(-b+y)^2+z^2)}{((-b+y)^2+z^2)((a+x)^2+(-b+y)^2+z^2)^{3/2}}\\[3mm]+\frac{(-a+x)(b+y)(2(-a+x)^2+(b+y)^2+z^2)}{((b+y)^2+z^2)((-a+x)^2+(b+y)^2+z^2)^{3/2}}-\frac{(a+x)(b+y)(2(a+x)^2+(b+y)^2+z^2)}{((b+y)^2+z^2)((a+x)^2+(b+y)^2+z^2)^{3/2}}\\[3mm]-\frac{(-a+x)(-b+y)(2(-a+x)^4+((-a+x)^2-z^2)((-b+y)^2+z^2))}{((-a+x)^2+z^2)^2((-a+x)^2+(-b+y)^2+z^2)^{3/2}}\\[3mm]+\frac{(-a+x)(b+y)(2(-a+x)^4+((-a+x)^2-z^2)((b+y)^2+z^2))}{((-a+x)^2+z^2)^2((-a+x)^2+(b+y)^2+z^2)^{3/2}}\\[3mm]+\frac{(a+x)(-b+y)(2(a+x)^4+((a+x)^2-z^2)((-b+y)^2+z^2))}{((a+x)^2+z^2)^2((a+x)^2+(-b+y)^2+z^2)^{3/2}}\\[3mm]-\frac{(a+x)(b+y)(2(a+x)^4+((a+x)^2-z^2)((b+y)^2+z^2))}{((a+x)^2+z^2)^2((a+x)^2+(b+y)^2+z^2)^{3/2}}\end{array}\right)$$

$$\sigma_{xy} = \frac{-Gb_z}{2\pi} \left(\frac{1}{\sqrt{(-a+x)^2+(-b+y)^2+z^2}} - \frac{1}{\sqrt{(a+x)^2+(-b+y)^2+z^2}} - \frac{1}{\sqrt{(-a+x)^2+(b+y)^2+z^2}} + \frac{1}{\sqrt{(a+x)^2+(b+y)^2+z^2}} \right) \frac{-Gb_z}{4\pi(1-\nu)}$$

$$\times \left(\begin{array}{l} -\dfrac{(-a+x)^2+z^2}{((-a+x)^2+(-b+y)^2+z^2)^{3/2}} + \dfrac{(a+x)^2+z^2}{((a+x)^2+(-b+y)^2+z^2)^{3/2}} \\[2mm] +\dfrac{(-a+x)^2+z^2}{((-a+x)^2+(b+y)^2+z^2)^{3/2}} - \dfrac{(a+x)^2+z^2}{((a+x)^2+(b+y)^2+z^2)^{3/2}} \\[2mm] -\dfrac{(-b+y)^2+z^2}{((-a+x)^2+(-b+y)^2+z^2)^{3/2}} + \dfrac{(b+y)^2+z^2}{((-a+x)^2+(b+y)^2+z^2)^{3/2}} \\[2mm] +\dfrac{(-b+y)^2+z^2}{((a+x)^2+(-b+y)^2+z^2)^{3/2}} - \dfrac{(b+y)^2+z^2}{((a+x)^2+(b+y)^2+z^2)^{3/2}} \end{array} \right)$$

$$\sigma_{zz} = \frac{-Gb_z}{4\pi(1-\nu)} \left(\begin{array}{l} -\dfrac{(-a+x)(-b+y)((-a+x)^4+z^2(3(-b+y)^2+4z^2)+(-a+x)^2((-b+y)^2+5z^2))}{((-a+x)^2+z^2)^2((-a+x)^2+(-b+y)^2+z^2)^{3/2}} \\[2mm] +\dfrac{(-a+x)(b+y)((-a+x)^4+z^2(3(b+y)^2+4z^2)+(-a+x)^2((b+y)^2+5z^2))}{((-a+x)^2+z^2)^2((-a+x)^2+(b+y)^2+z^2)^{3/2}} \\[2mm] +\dfrac{(a+x)(-b+y)((a+x)^4+z^2(3(-b+y)^2+4z^2)+(a+x)^2((-b+y)^2+5z^2))}{((a+x)^2+z^2)^2((a+x)^2+(-b+y)^2+z^2)^{3/2}} \\[2mm] -\dfrac{(a+x)(b+y)((a+x)^4+z^2(3(b+y)^2+4z^2)+(a+x)^2((b+y)^2+5z^2))}{((a+x)^2+z^2)^2((a+x)^2+(b+y)^2+z^2)^{3/2}} \\[2mm] -\dfrac{(-a+x)(-b+y)((-b+y)^4+z^2(3(-a+x)^2+4z^2)+(-b+y)^2((-a+x)^2+5z^2))}{((-b+y)^2+z^2)^2((-a+x)^2+(-b+y)^2+z^2)^{3/2}} \\[2mm] +\dfrac{(a+x)(-b+y)((-b+y)^4+z^2(3(a+x)^2+4z^2)+(-b+y)^2((a+x)^2+5z^2))}{((-b+y)^2+z^2)^2((a+x)^2+(-b+y)^2+z^2)^{3/2}} \\[2mm] +\dfrac{(-a+x)(b+y)((b+y)^4+z^2(3(-a+x)^2+4z^2)+(b+y)^2((-a+x)^2+5z^2))}{((b+y)^2+z^2)^2((-a+x)^2+(b+y)^2+z^2)^{3/2}} \\[2mm] -\dfrac{(a+x)(b+y)((b+y)^4+z^2(3(a+x)^2+4z^2)+(b+y)^2((a+x)^2+5z^2))}{((b+y)^2+z^2)^2((a+x)^2+(b+y)^2+z^2)^{3/2}} \end{array} \right)$$

$$\sigma_{yz} = \frac{-Gb_z}{4\pi(1-\nu)} \left(\begin{array}{l} \dfrac{(-a+x)z}{((-a+x)^2+(-b+y)^2+z^2)^{3/2}} - \dfrac{(-a+x)z}{((-a+x)^2+(b+y)^2+z^2)^{3/2}} \\[2mm] -\dfrac{(a+x)z}{((a+x)^2+(-b+y)^2+z^2)^{3/2}} + \dfrac{(a+x)z}{((a+x)^2+(b+y)^2+z^2)^{3/2}} \\[2mm] -\dfrac{(-a+x)z(2(-b+y)^4+(-b+y)^2((-a+x)^2+z^2)-z^2((-a+x)^2+z^2))}{((-b+y)^2+z^2)^2((-a+x)^2+(-b+y)^2+z^2)^{3/2}} \\[2mm] +\dfrac{(a+x)z(2(-b+y)^4+(-b+y)^2((a+x)^2+z^2)-z^2((a+x)^2+z^2))}{((-b+y)^2+z^2)^2((a+x)^2+(-b+y)^2+z^2)^{3/2}} \\[2mm] +\dfrac{(-a+x)z(2(b+y)^4+(b+y)^2((-a+x)^2+z^2)-z^2((-a+x)^2+z^2))}{((b+y)^2+z^2)^2((-a+x)^2+(b+y)^2+z^2)^{3/2}} \\[2mm] -\dfrac{(a+x)z(2(b+y)^4+(b+y)^2((a+x)^2+z^2)-z^2((a+x)^2+z^2))}{((b+y)^2+z^2)^2((a+x)^2+(b+y)^2+z^2)^{3/2}} \end{array} \right)$$

Here, σ_{yy} and σ_{xz} can both be obtained from σ_{xx} and σ_{yz}, respectively, by interchanging both x and y, and a and b. Note that the "prime" (see the inset of Fig. 3) has been removed from the x, y, and z symbols above for convenience.

References

[1] Yoffe, E., 1961, "A Dislocation at a Free Surface," Philos. Mag., **6**, pp. 1147–1155.
[2] Bacon, D. J., and Groves, P. P., 1970, "The Dislocation in a Semi-Infinite Isotropic Medium," *Fundamental Aspects of Dislocation Theory*, J. A. Simmons, R. de Witt, and R. Bullough, eds, Spec. Publ. 317, I, pp. 35–45.
[3] Groves, P. P., and Bacon, D. J., 1970, "The Dislocation Loop Near a Free Surface," Philos. Mag., **22**, pp. 83–91.
[4] Maurissen, Y., and Capella, L., 1974, "Stress Field of a Dislocation Segment Parallel to a Free Surface," Philos. Mag., **29**(5), pp. 1227–1229.
[5] Maurissen, Y., and Capella, L., 1974, "Stress Field of a Dislocation Segment Perpendicular to a Free Surface," Philos. Mag., **30**(3), pp. 679–683.
[6] Comninou, M., and Dunders, J., 1975, "The Angular Dislocation in a Half Space," J. Elast., **5**(3–4), pp. 203–216.
[7] Gosling, T. J., and Willis, J. R., 1994, "A Line-Integral Representation For the Stresses Due to an Arbitrary Dislocation in an Isotropic Half-Space," J. Mech. Phys. Solids, **42**(8), pp. 1199–1221.
[8] Lothe, J., Indenbom, V. L., and Chamrov, V. A., 1982, "Elastic Fields and Self-Force of Dislocations Emerging at the Free Surfaces of an Anisotropic Halfspace," Phys. Status Solidi B, **111**, pp. 671–677.
[9] Zbib, H. M., Rhee, M., and Hirth, J. P., 1998, "On Plastic Deformation and the Dynamics of 3D Dislocations," Int. J. Mech. Sci., **40**(2–3), pp. 113–127.
[10] Rhee, M., Zbib, H. M., Hirth, J. P., Huang, H., and de la Rubia, T., 1998, "Models for Long/Short-Range Interactions and Cross Slip in 3D Dislocation Simulation of BCC Single Crystals," Modelling Simul. Mater. Sci. Eng., **6**, pp. 467–492.
[11] Hirth, J. P., and Lothe, J., 1982, *Theory of Dislocations*, Krieger Publishing Company, Malabar, FL.
[12] Devincre, B., 1995, "Three-Dimensional Stress Field Expressions for Straight Dislocation Segments," Solid State Commun., **93**(11), pp. 875–878.
[13] Hills, D. A., Kelly, P. A., Dai, D. N., and Korsunsky, A. M., 1996, *Solution of Crack Problems: The Distributed Dislocation Technique*, Kluwer Academic Publishers, Dordrecht, The Netherlands.
[14] Khraishi, T. A., Hirth, J. P., Zbib, H. M., and Khaleel, M. A., 2000, "The Displacement, and Strain-Stress Fields of a General Circular Volterra Dislocation Loop," Int. J. Eng. Sci., **38**(3), pp. 251–266.
[15] Khraishi, T. A., Zbib, H. M., Hirth, J. P., and de la Rubia, T. D., 2000, "The Stress Field of a General Circular Volterra Dislocation Loop: Analytical and Numerical Approaches," Philos. Mag. Lett., **80**(2), pp. 95–105.
[16] Chapra, S., and Canale, R., 1998, *Numerical Methods for Engineers With Programming and Software Applications*, WCB McGraw-Hill, Boston.
[17] Khraishi, T., 2000, "The Treatment of Boundary Conditions in Three-Dimensional Dislocation Dynamics Analysis," PhD dissertation, Washington State University.
[18] Khraishi, T. A., Zbib, H. M., and de la Rubia, T. D., 2001, "The Treatment of Traction-Free Boundary Condition in Three-Dimensional Dislocation Dynamics Analysis Using Generalized Image Stress Analysis," Mater. Sci. Eng., A, **309–310**, pp. 283–287.